Half-time heat map reveals ultrasonic effects on morphology and kinetics of amyloidogenic aggregation reaction

Kichitaro Nakajima,[†,‖] Hajime Toda,[‡,‖] Keiichi Yamaguchi,[†] Masatomo So,[¶] Kensuke Ikenaka,[§] Hideki Mochizuki,[§] Yuji Goto,[†] and Hirotsugu Ogi[*,‡]

†*Global Center for Medical Engineering and Informatics, Osaka University, Suita, Osaka 565-0871, Japan.*

‡*Graduate School of Engineering, Osaka University, Suita, Osaka 565-0871, Japan.*

¶*Astbury Centre for Structural Molecular Biology, University of Leeds, Leeds LS2 9JT, UK.*

§*Department of Neurology, Graduate School of Medicine, Osaka University, Suita, Osaka 565-0871, Japan*

‖*Contributed equally to this work*

E-mail: ogi@prec.eng.osaka-u.ac.jp

Phone: +81 (6)6879 7276. Fax: +81 (6)6879 7276

Abstract

Ultrasonication has been recently adopted in amyloid-fibril assays because of its ability to accelerate the fibril formation, being promising in the early-stage diagnosis of amyloidoses in clinical applications. Although applications of this technique are expanding in the field of protein science, its effects on the aggregation reactions of amyloidogenic proteins are poorly understood. In this study, we comprehensively investigate the morphology and structure of resultant aggregates, kinetics of fibril formation, and seed-detection sensitivity under ultrasonication using β_2-microglobulin and compare these

characteristics under shaking, which has been traditionally adopted in amyloid-fibril assays. To discuss the ultrasonic effects on the amyloid-fibril formation, we propose the half-time heat map, which describes the phase diagram of the aggregation reaction of amyloidogenic proteins. The experimental results show that ultrasonication greatly promotes fibril formation, especially in dilute monomer solutions, induces short-dispersed fibrils, and is capable of detecting ultratrace seeds with a detection limit of 10 fM. Furthermore, we indicate that ultrasonication highly alters an energy landscape of the aggregation reaction due to the effect of ultrasonic cavitation. These insights contribute not only to our understanding of the effects of agitations on amyloidogenic aggregation reactions, but also to their effective application in the clinical diagnosis of amyloidoses.

Keywords

amyloid fibril, ultrasonication, shaking, supersaturation, seed detection, ultrasonic cavitation

Introduction

Amyloid fibrils are aggregates of proteins that exhibit a needle-like morphology(*1*) and are deeply involved in the pathology of amyloidoses, including Alzheimer's disease, Parkinson's disease, and dialysis-related amyloidosis(*2*). During the progress of amyloidosis, the causative proteins change their state from soluble monomers into toxic insoluble fibrils, which deposit on biological tissues and injure the tissues(*3*). Once the damage causes malfunction of tissues, it is difficult to completely cure them. In addition to amyloid fibrils, recent studies indicate that oligomeric aggregates, which appear in the early stage of the aggregation reaction, are also toxic agents in amyloidoses(*4*). Thus, it is critical to prevent formation of the toxic aggregates before the onset of clinical symptoms for mitigating amyloidoses.

Soluble monomers form insoluble fibrils through the primary-nucleation and subsequent fibril-elongation reactions(*5*). This process resembles the crystallization of an organic com-

pound in a supersaturated solution(*6–8*). The nucleation takes a long time, while the fibril elongation reaction rapidly proceeds from nuclei, as indicated by the seeding reaction(*9*). Because of the high energy barrier of the primary nucleation, experiments investigating physicochemical properties of amyloid fibrils require a long time. Therefore, a number of experimental studies adopted external stimuli to accelerate the fibril-formation reaction(*10*).

Shaking is one of the most common methods to accelerate the aggregation reaction(*11*). Especially, the intermittent shaking agitation is used in the real-time quaking-induced conversion (RT-QuIC) method(*12*), which receives attention as the early-stage diagnosis method of amyloidoses(*13*). Recently, ultrasonication has also been utilized as an acceleration method in amyloid-fibril assays. Ultrasonication has been used for fragmentating fibrils(*14*) and for the early-stage diagnosis of prion disease, which is called protein misfolding cyclic amplification (PMCA) method(*15*). Furthermore, our research group found that ultrasonication can drastically accelerate the spontaneous fibril formation from monomer solution even without the seeds(*16*), and we have developed ultrasonic instruments for amyloid-fibril assays(*17*, *18*). Herein, our ultrasonic instruments mainly evaluate the spontaneous fibril formation, whereas the RT-QuIC and PMCA methods detect the preexisting seeds by amplification. (Note that our ultrasonic instruments are also applicable for the seed detection(*18*, *19*).) Although ultrasonication and shaking are promising in the early-stage diagnosis of amyloidoses(*20*), the difference between their effects on the amyloidogenic aggregation reaction has not been understood.

In this study, we investigate the effects of ultrasonication and shaking on the aggregation reaction of β_2-microglobulin (β2m), which has been widely used in amyloid-fibril studies due to its clinical importance in dialysis-related amyloidosis(*21*). For the ultrasonication experiments, we used the laboratory-built ultrasonic instrument for the amyloid-fibril assays(*18*). It allows us to irradiate the sample solutions in a 96-well microplate with ultrasonic wave with the optimum frequency of 30 kHz, at which the maximum acceleration efficiency was obtained for the fibril-formation reaction(*22*). In this study, we further refine this instrument

to improve its reproducibility and study features of both spontaneous and seed-dependent amyloid-fibril formation induced by ultrasonication.

We systematically investigate relationships among morphology of resultant aggregates, the acceleration degree to the fibril-formation reaction, and β2m monomer and salt concentrations under quiescence, shaking, and ultrasonication. The properties of the aggregation reaction are discussed by a half-time heat map, which emerges the changes in the phase diagram by the agitations. The result reveals several characteristics in ultrasonically induced aggregation reaction that have not been previously known. For example, the amount of amorphous aggregates formed along with fibrils is reduced by ultrasonication, and ultrasonication shows a high acceleration effect on the fibril formation, especially, for dilute monomer solutions.

Furthermore, we perform the seeding experiments with ultratrace seeds under various agitations. The result shows that ultrasonication is capable of detecting the seeds with much lower concentration than the detection limit achieved by shaking, demonstrating the advantage of ultrasonication in the early-stage diagnosis of amyloidoses.

Finally, we discuss the physicochemical mechanism behind the acceleration capability of ultrasonication. Our results demonstrate that ultrasonication preferentially induces the fibril formation through monomer condensation by ultrasonic cavitation, dissolves kinetically trapped amorphous aggregates, and improves seed detection limit by selective seed fragmentation. These insights contribute to effectively applying the agitation to the clinical diagnosis of amyloidoses.

Results and Discussion

Reproducible amyloid-fibril assay using laboratory-built ultrasonic instrument

Because the fibril-formation kinetics is highly sensitive to the ultrasonic condition(*22*), achieving the high reproducible assay with ultrasonication requires accurate control of the acoustic condition in the sample solution. As described in SI appendix 1 in detail, we originally developed the ultrasonic instrument for the amyloid-fibril assays (Figure 1)(*18*). In this study, we further improved the uniformity of the assay in terms of the half time (t_{half}) of the thioflavin-T (ThT) fluorescence curves, which is the time when the ThT fluorescence intensity becomes half of its maximum. Consequently, the ultrasonication assay achieved the reproducibility in the ThT kinetics (Figure S1), which is equivalent to that of the shaking assay, allowing us to discuss the difference in the effects on the amyloidogenic aggregation reactions between ultrasonication and shaking.

Difference in aggregates formed under various agitations

We analyzed the secondary structure and morphology of aggregates formed in solutions with various salt concentrations under quiescence, shaking, and ultrasonication. The morphology of aggregates, including amyloid fibrils and amorphous aggregates, formed from supersaturated solutions depends on the salt concentration(*6*, *23*), and we varied the salt concentration to evaluate how the agitations affect the supersaturation state. The circular dichroism (CD) spectra of the prepared acidic monomer solutions with the monomer concentration of 0.3 mg/mL in the 20-mM HCl with different salt concentrations are shown in Figure 2a, which are similar regardless of the salt concentration and are identical to that of the acid denatured β2m monomers(*23*). Figure 2b-g show the CD spectra and atomic force microscopy (AFM) images of the formed aggregates under quiescence, shaking, and ultrasonication. In addition, the ThT time-course curves during the aggregation reaction

are shown in Figure 3a-c.

Under quiescence, the monomer in the solution with 30-mM NaCl remains soluble for 100 h. At increased salt concentrations (i.e., 80, 150, and 240 mM), their CD spectra show a negative peak near 218 nm, implicating the formation of the fibrils with β-sheet structures(*24*). The AFM images demonstrate the formation of the fibril-like morphology with the diameter of $\sim$7 nm (Figure S2), and the ThT time-course curves follow a typical sigmoidal function. We note that the ThT time-course of the 240-mM NaCl (green curves in Figure 3a) shows a deformed sigmoidal curve, where the ThT level continues to increase after the first precipitous increase. In addition, the AFM image shows small globular aggregates along with the fibrils. These observations indicate formation of amorphous aggregates in this condition. Further increase in the salt concentration (i.e., 480 mM) induces short worm-like aggregates, and its solution shows an aberrant CD spectrum that is quite different from the typical spectrum observed for a solution with fibrils. In addition, the ThT fluorescence intensity of the solution with these aggregates remains low, suggesting that aggregates formed in the 480-mM-NaCl solution are the aggregates different from the amyloid fibrils. In this study, the aggregates are categorized into two groups, the amyloid fibrils and amorphous aggregates. The former is characterized by the negative peak near 218 nm in the CD spectrum, the height between 5 to 10 nm in the AFM image, and the sigmoidal function in the ThT fluorescence time-course curve. In contrast, we consider aggregates different from the amyloid fibrils as the amorphous aggregates. As discussed below, the amorphous aggregates include metastable curvilinear fibrils(*25*, *26*). These definitions are important to discuss the energy landscape of the amyloidogenic aggregation reaction under agitations.

Concerning the shaking assay, the morphology of the formed aggregates presents mature fibrils with length over 1 μm at low salt concentrations (i.e., 30, 80, and 150 mM). Also, their CD spectra and ThT time-course curves indicate formation of the β-sheet-rich amyloid fibrils (Figure 2c and Figure 3b) with the diameter of $\sim$7 nm (Figure S2). The amyloid fibrils are formed by shaking even with 30-mM NaCl, whereas the fibril formation fails to

occur under quiescence with this salt concentration. The AFM image of the aggregates formed in the solution with 240-mM NaCl shows small globular aggregates in addition to the fibrils (Figure S3). Furthermore, the fibril-like morphology is rarely observed in 480-mM-NaCl solution. Instead of the fibrils, short worm-like aggregates, so-called curvilinear fibrils(*25*, *26*), are observed in abundance. Consistent with the AFM observation, the CD spectra indicate a decrease in the β-sheet structure for high-salt concentration solutions. It should be noted that formation of the amorphous aggregates without ordered structures shifts the CD spectrum for the β-sheet-structure spectrum to the random-coil-structure spectrum. However, we observed a decrease in the negative-peak intensity at 218 nm, but not a shift in the wavelength. Previously, we reported that the formation of amorphous aggregates disturbs the CD spectrum measurement(*27*), because the amorphous aggregates scatter the incident light. This fact complicates the interpretation of the CD spectrum of the sample solution including amorphous aggregates, preventing us from quantitatively analyzing the secondary structure from the CD spectrum(*28*, *29*). We thus consider that the decrease in the negative-peak intensity at 218 nm is caused by the formation of amorphous aggregates.

Ultrasonication induced the fibrils in low salt-concentration solutions (i.e., 30, 80, and 150 mM). Their CD spectra show that the formed short fibrils possess the β-sheet-rich structure (Figure 2d). They show the short and dispersed morphology (Figure 2g), being attributed to the strong fragmentation effect(*30*). Their diameter is identical to that of fibrils formed by quiescence and shaking (Figure S2). Although the further increase in the salt concentration to 240 mM results in the formation of the amorphous aggregates under quiescence and shaking, they are not observed in the ultrasonicated sample (Figure 2g). In addition to the AFM image, the CD spectrum and ThT time-course curve also indicate formation of the β-sheet-rich fibrils (Figure 2d), that is different from the results for quiescence and shaking. Even in the sample with 480-mM NaCl, the fibrils coexist with the globular amorphous aggregates. The CD spectrum also supports the fibril formation even in such a high salt concentration by the 218-nm negative peak. Aggregates formed under the

three agitations are summarized in Table 1. It is difficult to determine the exact amount of formed amorphous aggregates. However, their presence has been reliably assessed by the AFM observations of the globular aggregates on the surface of the fibrils, decrease in the negative-peak intensity near 218 nm in the CD spectra, and shift of the ThT time-course curves from the typical sigmoidal curve to deformed sigmoidal curve, and this information is sufficient to make a useful discussion. The difference in resultant aggregates under ultrasonication and shaking is attributed to the difference in their aggregation acceleration mechanisms, that is discussed in the following section.

ThT time-course under various agitations

We performed the ThT time-course measurement for solutions with various monomer concentrations between 0.01 and 1.0 mg/mL under quiescence, shaking, and ultrasonication. The results are summarized in Figure 3d-f using the t_{half} value of individual curves. Results for samples, in which the ThT intensity failed to increase within 100 h, are plotted at 100 h (Figure 3d-f), and we regarded that they would never cause the fibril formation. This definition is for the sake of expediency to discuss the metastable region in the thermodynamic phase diagram below.

At lower salt concentrations (i.e., 30, 80, and 150 mM), the t_{half} value shows an inverse correlation with the monomer concentration under quiescence and shaking, except for data of t_{half} =100 h, as expected (Figure 3d,e). At higher salt concentrations (i.e., 240 and 480 mM), higher monomer-concentration samples show equivalent or longer t_{half} values to those of lower ones. In these conditions, the resultant aggregates show the amorphous morphology. In addition, Hasecke and co-workers reported that slower ThT kinetics in higher-protein-concentration solutions is attributed to the amorphous (oligomeric) species(*31*). Therefore, a longer t_{half} value in the region with higher monomer and higher salt concentrations indicates formation of the amorphous aggregates. As a possible mechanism, once the amorphous aggregates are partially formed, the concentration of active free monomers decreases in the

solution, leading to the slow kinetics of the fibril formation. Another view for the cause of the slow kinetics is the slow conversion of rapidly formed amorphous aggregates to mature fibrils as discussed previously(*23*).

In the case of ultrasonication (Figure 3f), only the samples with 30-mM NaCl show a monotonic decrease in the t_{half} value as the increase in the monomer concentration. For NaCl concentrations of 80, 150, and 240 mM, the t_{half} value decreases in the lower monomer-concentration region. However, the t_{half} values are nearly the same ($\sim$10 h) regardless of the monomer concentration in the higher monomer-concentration region, implicating that the acceleration effect of ultrasonication saturates at those conditions. In the samples with 480-mM NaCl, the t_{half} value increases as the monomer concentration increases due to formation of the amorphous aggregates. This trend appears to be similar to that under shaking. However, the t_{half} values of these samples under ultrasonication are considerably shorter than those under shaking, presumably indicating the rapid conversion from the amorphous aggregates to the fibrils under ultrasonication.

Half-time heat map and phase diagram

To visually compare the effects among under quiescence, shaking, and ultrasonication on the aggregation reaction, the thermodynamic phase diagrams are depicted based on the half-time (t_{half}-value) heat map (Figure 4a-c), where the four regions previously indicated in the phase diagram stand out(*6*): (I) Soluble region, where the protein concentration is less than its intrinsic solubility. In other words, the solution is unsaturated, and formation of aggregates never happens. (II) Metastable region, where the protein solution is in supersaturation with a concentration above the solubility, but the spontaneous nucleation fails to occur. Thus, the monomers in the solution remain in the soluble state in supersaturation. (III) Labile region, where the solution is in supersaturation, and amyloid fibrils are formed through the spontaneous nucleation after a lag time. In this region, the dominant product is the amyloid fibril. And (IV) Amorphous region, where the monomers immediately precipitate

as amorphous aggregates owing to a very high degree of the driving force. In this region, the dominant product is the amorphous aggregate.

To draw the boundary between the soluble and metastable regions, the solubility of acidic β2m solution is measured as described in Materials and Methods. Because the protein solubility depends on the salt concentration(*32*), the solubility is determined with different four salt concentrations and is plotted in Figure 4a-c. As mentioned above, we here define the metastable region as the condition, where the fibril formation fails to occur within 100 h. The boundary between the labile and amorphous regions indicates the formation of the amorphous aggregates.

Under shaking (Figure 4b), the metastable region becomes narrower than that under quiescence (Figure 4a), showing that shaking induces downward shift of the metastable-labile boundary, whereas the labile-amorphous boundary is little affected. On the other hand, ultrasonication causes not only the significant downward shift of the metastable-labile boundary, but also the upward shift of the labile-amorphous boundary (Figure 4c). The difference in the phase diagram is attributed to the difference in the aggregation acceleration mechanism between ultrasonication and shaking, as discussed in detail below.

It is striking that, in the labile region, although the acceleration ability of shaking is similar to that of ultrasonication for solutions of high-monomer concentrations, it deteriorates for solutions of monomer concentration lower than 0.1 mg/mL. The aggregation acceleration by shaking results from the increase in the apparent mean-free path of the monomer movements. Thus, shaking enhances probability of the intermolecular interactions in a condensed solution by increasing a collision frequency among monomers. However, it fails to increase the collision frequency in a dilute solution, diminishing the acceleration effect for nucleation.

In contrast, ultrasonication keeps the high acceleration ability even for dilute monomer solutions. In the aggregation acceleration mechanism, the cavitation bubble works as a catalyst for the nucleation reaction(*22*, *33*); the cavitation bubbles are generated by the negative pressure of ultrasound, which attract the monomers on the bubble surface during

the bubble expansion phase because the hydrophobic amino acid residues prefer the air-water interface(*34*). The subsequent bubble collapse condenses the monomers attached on the bubble surface into the collapse center and locally and transiently heats the solution, promoting the nucleation reaction(*22*). The bubbles typically expand their radius of the order of 10 μm and shrink in the radius less than 1 μm, resulting in the change in the volume by a factor over 1000. This drastic volume change causes a local and instantaneous increase in the monomer concentration near the bubble-collapse point, accelerating the nucleation reaction even in the dilute monomer solutions. On the other hand, if the bubble surface becomes absolutely covered with the monomers, the aggregation acceleration effect saturates. This fact consistently explains the reason why the t_{half} value of the samples cannot be decreased below the lower limit of $\sim$10 h for solutions with high-monomer concentrations by ultrasonication (Figure 3f), indicating the saturation of the acceleration effect of ultrasonication.

Seeding reaction under various agitations

We also investigated the effects of ultrasonication and shaking on the seeding reaction. Because the ultratrace seeds (less than 1 nM) are detected in the biological fluids in the early-stage of amyloidoses(*13*), the rapid and sensitive seed-detection method is desired in clinical applications. So far, the RT-QuIC and PMCA methods have indicated their applicability for the early stage diagnosis of amyloidoses(*13*, *20*). However, the difference between two methods has not been fully discussed.

Here, we prepared 0.03-mg/mL β2m monomer solutions with 150-mM NaCl, being in the labile region, and added the seeds with concentrations between 10 fM and 10 nM. (Note that the seed concentration is a monomer equivalent concentration.) Representative time-course curves in the ThT-fluorescence measurement under quiescence, shaking, and ultrasonication are shown in Figure 5a-c, respectively. The t_{half} value at each condition is summarized in Figure 5d.

Without seeds, the t_{half} value for the fibril-formation reaction is $\sim$44 h under quiescence

(Figure 5a). By adding 10-nM seeds, it is shortened to be ∼4 h, indicating that the added seeds work as templates of the fibril growth. With the 10-pM seeds, the effect of seeds is clearly observed. However, the seeding effect becomes insignificant in the samples with the seed concentrations of 10 and 100 fM. Here, we calculated the seed detection limit by the following procedure. The average and standard deviation (SD) of the t_{half} value for each seed concentration were calculated, including for the monomer solution. The detection limit was then determined as the minimal seed concentration whose average ± 1SD do not overlap with that of the monomer solution. Based on this definition, the seed detection limit is 1 pM under quiescence.

The seeding reactions are accelerated for all seed concentrations by shaking (Figure 5b) compared to the reaction under quiescence, resulting in the rapid seed detection. However, the ThT time-course curves of the samples with the seed concentrations of 10 and 100 fM overlap the curve of the samples without seeds as with the assay under quiescence. Therefore, the seed detection limit is also 1 pM under shaking. This fact demonstrates that shaking accelerates the fibril formation, but cannot improve the detection limit.

Ultrasonication results in further acceleration of the seeding reaction (Figure 5c). Noteworthy, the ThT curve of the sample with the 10-fM seeds is clearly separated from that without seeds, showing the seed detection limit less than 10 fM under ultrasonication. This fact indicates that the seeding assay under ultrasonication is less time-consuming and more sensitive than shaking, being an important advantage in clinical applications.

At a high seed concentration, the fibril elongation from seed termini is a dominant reaction in the solution because the primary nucleation is bypassed by the seeds. In this case, a time required for the seed detection is determined by the fibril-elongation rate, which depends on rates of the two reactions; (i) attachment of monomers to the fibril termini and (ii) fragmentation of a long fibril into shorter ones. It should be noted that fragmentation of fibrils possibly promotes the reassociation of fibril fragments because of the increase in the number density of the fibril termini. Although this reaction can increase the average length of the

fibrils, the total number of the fibrils remains unchanged in the solution, meaning that this reaction is not detected by the ThT fluorescence. Thus, in this study, only the attachment of monomers to the fibril termini was taken into account in the fibril-elongation reaction. The former can be accelerated by stirring, since it increases the frequency of the collision between fibril termini and monomers. The latter increases the number of the fibril termini, amplifying the active seed number. The two reactions are enhanced by both ultrasonication and shaking, accelerating the seeding reaction compared to that under quiescence.

At an ultratrace seed concentration, the primary nucleation equally contributes to the fibril-formation reaction because the number of free monomers, which fail to react with the seeds, is abundant. When the seed concentration is below the detection limit, the fibril formation is dominated by the primary nucleation regardless of the seeds. Therefore, it is important to amplify the active seed number relative to the excess monomers through fragmentation of the seeds. Under shaking, previous reports indicate that fragmentation is induced by the shear-stress field caused by the fluid flow(*35*). The fragmentation effect under shaking is less significant than under ultrasonication, while the fluid flow accelerates the primary nucleation as well. Thus, shaking accelerates the fibril-formation reaction but fails to improve the detection limit. On the other hand, we previously reported that ultrasonication enhances both the primary nucleation and fragmentation reactions through the effects of cavitation bubbles(*18*). In the solution including the seeds, cavitation bubbles are selectively generated on the surface of the seeds, because hydrophobic amino acid residues at the fibril surface can be nuclei of the bubble(*36*). The generated bubble eventually collapses, resulting in fragmentation of the fibrils through a generation of shockwave(*37*). Therefore, ultrasonication can specifically break the seeds into shorter ones via ultrasonic cavitation. Simultaneously, ultrasonication accelerates the primary nucleation in the solution. However, the fragmentation effect preferentially occurs relative to the primary nucleation unlike the case of shaking, amplifying the active seed termini even in the case of the ultratrace seeds. The selective seed amplification improves the seed detection limit, being an important ad-

vantage in the clinical applications.

Energy landscape of the aggregation reaction

The systematic investigation of the morphology and structure of resultant aggregates reveals that the fraction of the amorphous aggregates decreases under ultrasonication compared to shaking. Usually, the amorphous aggregates originate in solutions with high protein and salt concentrations(*6*, *26*), where the driving force for precipitation is high. It is controversial whether the amorphous aggregate appears as an on-pathway intermediate for the amyloid fibril or it is an off-pathway dead-end product different from the fibril(*38*). We previously indicated that the β2m amorphous aggregate is the off-pathway aggregate, which is in a kinetically-trapped state(*23*). Moreover, Miti and coworkers suggested the thermodynamic landscape including the amorphous aggregates as an off-pathway competitor in the fibril formation of lysozyme and dimeric Aβ variant(*26*, *31*). We consider that the amorphous aggregate is the competitive off-pathway product and schematically explain the difference in the aggregation reactions under ultrasonication and shaking (Figure 6).

At lower salt concentrations, the free energy of soluble monomer state in a supersaturated solution will be lower than that of the amorphous state (Figure 6a), and when the driving force (i.e., protein monomer and salt concentrations) is insufficient to overcome the energy barrier for nucleation, the monomers remain soluble in a supersaturation state. This corresponds to the metastable region in the phase diagram (Figure 4a). In the labile region, however, the monomer state eventually moves to the fibril state because of a sufficient driving force to overcome the barrier. Thus, the amyloid fibrils form via spontaneous nucleation with a lag time in the labile region. Agitation can decrease the apparent energy barrier for nucleation, shifting the metastable-labile boundary downward (Figure 4b,c). After the nucleation, the fibrils elongate because the longer fibrils are more stable than shorter ones.

The higher the salt concentration, the more stable amorphous aggregates accumulate. In addition, because the energy barrier for formation of the amorphous aggregate is much lower

than that for fibril formation(*23*), the amorphous aggregates are rapidly formed without a lag time(*6*, *39*). Thus, the amorphous aggregates are preferentially formed under shaking at higher salt concentrations regardless of their less stability than the fibrils, corresponding to the amorphous-region in the phase diagram. As Hasecke and coworkers reported(*40*), the kinetically trapped oligomeric aggregates can work as an inhibitor for the fibril formation. Therefore, the progress of the amorphous-aggregate formation prevents the monomers from forming the fibrils.

All experimental observations in this study can be consistently explained by considering that the energy landscape can vary depending on the kinds of agitation as shown in Figure 6b. In contrast to shaking, ultrasonication results in a different effect on each reaction pathway: (i) For the nucleation reaction, ultrasonication drastically decreases the energy barrier for nucleation through the catalytic effect of the cavitation bubbles(*22*) (Figure 6c). (ii) For the fibril elongation reaction, shorter fibrils become more stable under the ultrasonic field relative to longer ones, resulting in homogeneous fibril fragments(*30*, *36*) (Figure 6d). (iii) Ultrasonication can dissolute the amorphous aggregates into soluble monomers by the dispersion effect(*41*), leading to an increase in the apparent energy barrier for the amorphous-aggregate formation. This effect can shift the labile-amorphous boundary upward (Figure 4c). Aforementioned three effects contribute to the preferential formation of short fibril fragments rather than longer fibrils and amorphous aggregates at an accelerated rate.

The difference in the effects between ultrasonication and mechanical agitation is often discussed in the field of sonochemical (i.e., ultrasonically induced) crystallization. For instance, the resultant crystals of alum under ultrasonication show morphology of smaller and more uniform crystal-size distribution than that under mechanical stirring due to the effects of cavitation bubbles(*42*), resembling our observations of the amyloid-fibril morphology. Furthermore, in the synthesis of magnetite nanoparticles, it is reported that ultrasonication helps the synthesis of themodynamically stable products through the dissolution of metastable precipitates, which is rapidly formed in the initial phase of the synthesis(*43*, *44*).

The slow formation of thermodynamically stable crystals following the rapid formation of metastable amorphous precipitates is often seen in crystallization systems(*45*, *46*), known as Ostwald ripening: Supersaturated solutes first form amorphous precipitates because of their lower energy barrier for precipitation (i.e., rapid kinetics). However, once the crystal nucleation happens in the solution, the amorphous precipitates can transform their state into stable crystals via the dissolution of constituent monomers. Actually, dissolution of an amorphous precipitate proceeds with a lower reaction rate, preventing the monomers from forming crystals quickly. During this process, ultrasonication assists the dissolution of metastable precipitates, resulting in crystallization of the supersaturated solutes(*43*). When we see the relationship between the amyloid fibrils and amorphous aggregates through a phase diagram based on the half-time heat map, the ultrasonic effects on the amyloidogenic aggregation reaction can be explained as analogous to the general mechanism in the sonochemical crystallization.

Conclusions

We comprehensively investigated the effects of ultrasonication and shaking on the amyloid-fibril formation, which are important methodologies in the early-stage diagnosis of amyloidoses. The ultrasonication assay was performed using the laboratory-built ultrasonic instrument, which achieved highly reproducible assay. The experimental results revealed that; (i) ultrasonication preferentially formed short and dispersed fibril fragments through fragmentation of the fibrils and dissolved the metastable amorphous aggregates; (ii) although the acceleration capability for the fibril formation of shaking deteriorates in the dilute monomer solutions, ultrasonication effectively accelerates the fibril formation even in dilute monomer solutions; and (iii) ultrasonication improves the seed detection limit with the high acceleration effect. In the phase diagram based on the half-time heat map, ultrasonication alters the boundary not only between the metastable and labile regions, but also between the labile

and amorphous regions. These results clearly revealed the difference in the effect between ultrasonication and shaking, contributing to the further understanding of the role of agitations in the amyloid-fibril assays.

Materials and Methods

Preparation of the sample solution

The wild type β2m monomers were expressed in *Escherichia Coli* and purified by the procedure described previously(*47*). Note that the β2m monomer expressed in *Escherichia Coli* has a methionine residue at the N-terminal in addition to the wild-type sequence. The obtained β2m monomers were lyophilized and kept at -20 °C. The lyophilized powder β2m monomer was first dissolved by a 10-mM HCl solution. The β2m concentration in the solution was determined using the absorbance measurement at 280 nm of 1.93×10^4 $M^{-1}{\cdot}cm^{-1}$. The monomer solution was then filtered by a membrane filter with the pore diameter of 220 nm (Millipore, SLGVR04NL) to remove larger aggregates if any. The monomer solution was mixed with HCl, ThT dye, and NaCl. The final concentration of each component is as follows; 0.01-1.0 mg/mL β2m, 20 mM HCl, 5 μM ThT, and 30-480 mM NaCl. In the seeding assay, the preformed β2m fibrils were used as seeds. The seed solution was treated with the ultrasonic homogenizer (Misonix, XL-2000) to break them down into short fragments and was immediately added to the monomer solution as previously described(*18*).

Ultrasonication assay

We have originally developed the ultrasonic instrument (Figure 1), which is optimized for the accelerative amyloid-fibril assay(*18*). The prepared sample solutions with the volume of 198 μL were dispensed into a 96-well microplate (Greiner, 675096). The sample solutions were sealed by a plastic film with a thickness of 0.1 mm (WATSON, 547-KTS-HC). Piezoelectric lead zirconate titanate (PZT) transducers were placed on the plastic film, where the

film surface is covered by an acoustic couplant gel (ECHO ultrasonics, EchoPure^{TM}). The single PZT transducer was independently positioned on each sample solution. The solution temperature was kept at 37 °C.

The PZT transducer measures $4.24 \times 4.24 \times 54$ mm^3, whose resonant frequency (fundamental longitudinal vibration) is ∼30 kHz that is the optimum frequency for accelerating the fibril-formation reaction(*22*). The PZT material (Fuji Ceramics Corp., P213-C) shows a piezoelectric constant d_{31} of -1.39×10^{-10} m·V^{-1}. The transducer resonates in its longitudinal direction by the transverse piezoelectric effect. The resonant frequency of each transducer was measured by obtaining the acoustic-intensity spectrum between 28 and 32 kHz using a microphone beneath the microplate. The representative spectrum is shown in the inset of Figure 1. Each transducer was driven by tone bursts for 0.3 s and remained unexcited for 28.5 s in a sequential manner (a duty ratio is ∼1%).

During the ultrasonication assay, the ThT fluorescence intensity of each sample solution was measured by the fluorospectrometer incorporated in the instrument. Because the ThT molecules specifically bind to the fibrils and emit strong fluorescence(*48*), an increase in the ThT fluorescence intensity corresponds to the increase in the fibril amount in the solution. The excitation and emission wavelengths of the ThT fluorescence measurement are 450 and 492 nm, respectively. The fluorescence measurement was performed every 10 min.

Shaking assay

We used the commercially available microplate reader (Corona Electric Co., SH-9000) for the assay under the shaking agitation. The 100-μL sample solutions were dispensed into the 96-well plate. The 96-well plate was shaken at 850 rpm with the cycle of 1-min shaking and 29-min incubation, which is typically adopted in the RT-QuIC assays(*13*, *49*). The ThT fluorescence intensity of each sample solution was measured every 10 min with the excitation and emission wavelengths of 450 and 492 nm, respectively. The sample solution temperature was kept at 37 °C.

AFM observation

The morphology of the formed aggregates was observed using an AFM system (HITACHI, AFM5000II). The sample solution with the β2m concentration of 0.3 mg/mL was diluted 10-fold with ultrapure water, and 15-μL solution was incubated on a mica plate for 1 min. After the surface was dried, AFM images were acquired using the tapping mode.

CD spectrum measurement

The secondary structure of the formed aggregates was analyzed using the CD spectrometer (JASCO Corp., J-820). After the aggregation assay, the concentraion of the sample solution was adjusted to 0.15 mg/mL by diluting it with ultrapure water. The 170-μL solution was injected into a quartz cell (JASCO Corp., 1103-0172) with a light path of 1 mm. The spectrum was acquired in the wavelength between 200 and 250 nm.

Measurement of solubility

When the solution reaches the equilibrium state after precipitation, the soluble monomer concentration equals the solubility. Thus, we determined the solubility by ultracentrifugating the fibril-formed solution to settle down the insoluble aggregates, and then, quantitating the monomer concentration in the supernatant using an enzyme-linked immunosorbent assay (ELISA) method(*50*).

We previously confirmed that aggregates, including fibrils and amorphous aggregates, in the solution settle out and form the pellet by the ultracentrifugation with the condition of 72,000$\times g$ for 30 min(*50*). In this study, the sample solution after the fibril-formation experiment using ultrasonication was ultracentrifugated for 60 min with 100,000$\times g$, which is the modified condition to settle out smaller aggregates as possible. We expect that the solution only monomers is obtained from the supernatant. However, very small oligomers, like dimers, could remain in the supernatant, which could affect the solubility measurement,

471 although their effect will be insignificant in the discussion because of the wide monomer-
472 concentration range of solubility measurement. After ultracentrifugation, the supernatant
473 was recovered. Because the supernatant solution was in the acidic condition, the pH of the
474 solution was adjusted to the neutral pH using 10-mM phosphate buffer (pH 7.4). After the
475 pH adjustment, the β2m monomer concentration in the supernatant was quantitated using
476 commercially-available kit (hB2M, Parameter Kit, R&D Systems, Inc.).

477 Conflicts of interest

478 There are no conflicts to declare.

479 Author Contribution

480 ‖K. N. and H. T. contributed equally. K. N. and H. T. performed ultrasonication and shaking
481 experiments, seeding experiments, analyzed the data, and wrote the manuscript. K. Y. and
482 M. S. established the experimental methods and performed AFM observation, CD spectrum
483 measurement, and solubility measurement. K. I. and H. M. contributed to the construction
484 of the optimized sonoreactor. Y. G. designed the research work and revised the manuscript.
485 H. O., the corresponding author, was responsible for managing the whole research project
486 and wrote the manuscript.

487 Supporting Information

488 The Supporting Information is available free of charge.

489 - SI Appendix 1: Reproducible amyloid-fibril assay using laboratory-built
490 ultrasonic instrument, where the reproducibility of quiescent incubation,
491 shaking, and ultrasonication assay is discussed (Figure S1).

492 - SI Appendix 2: Detailed analysis of AFM images (Figures S2 and S3).

Acknowledgement

This study was supported by the Japan Society for the Promotion of Science (20K22484), MDD Grant 2020 by the global center for medical engineering and informatics of Osaka University, Core-to-Core Program A (Advance Research Networks), Ministry of Education, Culture, Sports, Science and Technology (17H06352), and SENTAN from AMED (16809242).

References

1. Eisenberg, D. S., and Sawaya, M. R. (2017) Structural Studies of Amyloid Proteins at the Molecular Level. *Annu. Rev. Biochem. 86*, 69–95.

2. Chiti, F., and Dobson, C. M. (2017) Protein Misfolding, Amyloid Formation, and Human Disease: A Summary of Progress Over the Last Decade. *Annu. Rev. Biochem. 86*, 27–68.

3. Knowles, T. P., Vendruscolo, M., and Dobson, C. M. (2014) The amyloid state and its association with protein misfolding diseases. *Nat. Rev. Mol. Cell Biol. 15*, 384–396.

4. Stroud, J. C., Liu, C., Teng, P. K., and Eisenberg, D. (2012) Toxic fibrillar oligomers of amyloid-β have cross-β structure. *Proc. Natl. Acad. Sci. U.S.A. 109*, 7717–7722.

5. Morris, A. M., Watzky, M. A., Agar, J. N., and Finke, R. G. (2008) Fitting Neurological Protein Aggregation Kinetic Data via a 2-Step, Minimal/'Ockham's Razor' Model: The Finke-Watzky Mechanism of Nucleation Followed by Autocatalytic Surface Growth. *Biochemistry 47*, 2413–2427.

6. Yoshimura, Y., Lin, Y., Yagi, H., Lee, Y.-H., Kitayama, H., Sakurai, K., So, M., Ogi, H., Naiki, H., and Goto, Y. (2012) Distinguishing crystal-like amyloid fibrils and glass-like amorphous aggregates from their kinetics of formation. *Proc. Natl. Acad. Sci. U.S.A. 109*, 14446–14451.

7. So, M., Hall, D., and Goto, Y. (2016) Revisiting supersaturation as a factor determining amyloid fibrillation. *Curr. Opin. Struct. Biol. 36*, 32–39.

8. Noji, M., Samejima, T., Yamaguchi, K., So, M., Yuzu, K., Chatani, E., Akazawa-Ogawa, Y., Hagihara, Y., Kawata, Y., Ikenaka, K., Mochizuki, H., Kardos, J., Otzen, D. E., Bellotti, V., Buchner, J., and Goto, Y. (2021) Breakdown of supersaturation barrier links protein folding to amyloid formation. *Commun. Biol. 4*, 120, 1–10.

9. Jarrett, J. T., and Lansbury, P. T. (1993) Seeding "one-dimensional crystallization" of amyloid: A pathogenic mechanism in Alzheimer's disease and scrapie? *Cell 73*, 1055–1058.

10. Grigolato, F., Colombo, C., Ferrari, R., Rezabkova, L., and Arosio, P. (2017) Mechanistic Origin of the Combined Effect of Surfaces and Mechanical Agitation on Amyloid Formation. *ACS Nano 11*, 11358–11367.

11. Ladner-Keay, C. L., Griffith, B. J., and Wishart, D. S. (2014) Shaking Alone Induces De Novo Conversion of Recombinant Prion Proteins to β-Sheet Rich Oligomers and Fibrils. *PLOS ONE 9*, e98753, 1–12.

12. Atarashi, R., Satoh, K., Sano, K., Fuse, T., Yamaguchi, N., Ishibashi, D., Matsubara, T., Nakagaki, T., Yamanaka, H., Shirabe, S., Yamada, M., Mizusawa, H., Kitamoto, T., Klug, G., McGlade, A., Collins, S. J., and Nishida, N. (2011) Ultrasensitive human prion detection in cerebrospinal fluid by real-time quaking-induced conversion. *Nat. Med. 17*, 175–178.

13. Shahnawaz, M., Mukherjee, A., Pritzkow, S., Mendez, N., Rabadia, P., Liu, X., Hu, B., Schmeichel, A., Singer, W., Wu, G., Tsai, A. L., Shirani, H., Nilsson, K. P. R., Low, P. A., and Soto, C. (2020) Discriminating α-synuclein strains in Parkinson's disease and multiple system atrophy. *Nature 578*, 273–277.

14. Naiki, H., Hashimoto, N., Suzuki, S., Kimura, H., Nakakuki, K., and Gejyo, F. (1997) Establishment of a kinetic model of dialysis-related amyloid fibril extension in vitro. *Amyloid 4*, 223–232.

15. Saborio, G. P., Permanne, B., and Soto, C. (2001) Sensitive detection of pathological prion protein by cyclic amplification of protein misfolding. *Nature 411*, 810–813.

16. Ohhashi, Y., Kihara, M., Naiki, H., and Goto, Y. (2005) Ultrasonication-induced amyloid fibril formation of β2-microglobulin. *J. Biol. Chem. 280*, 32843–32848.

17. Umemoto, A., Yagi, H., So, M., and Goto, Y. (2014) High-throughput analysis of ultrasonication-forced amyloid fibrillation reveals the mechanism underlying the large fluctuation in the lag time. *J. Biol. Chem. 289*, 27290–27299.

18. Nakajima, K., Noi, K., Yamaguchi, K., So, M., Ikenaka, K., Mochizuki, H., Ogi, H., and Goto, Y. (2021) Optimized sonoreactor for accelerative amyloid-fibril assays through enhancement of primary nucleation and fragmentation. *Ultrason. Sonochem. 73*, 105508.

19. Kakuda, K., Ikenaka, K., Araki, K., So, M., Aguirre, C., Kajiyama, Y., Konaka, K., Noi, K., Baba, K., Tsuda, H., Nagano, S., Ohmichi, T., Nagai, Y., Tokuda, T., El-Agnaf, O. M., Ogi, H., Goto, Y., and Mochizuki, H. Ultrasonication-based rapid amplification of α-synuclein aggregates in cerebrospinal fluid. *Sci. Rep. 9*, 6001, 1–10.

20. Parnetti, L., Gaetani, L., Eusebi, P., Paciotti, S., Hansson, O., El-Agnaf, O., Mollenhauer, B., Blennow, K., and Calabresi, P. (2019) CSF and blood biomarkers for Parkinson's disease. *Lancet Neurol. 18*, 573–586.

21. Gejyo, F., Homma, N., Suzuki, Y., and Arakawa, M. (1986) Serum Levels of β2-Microglobulin as a New Form of Amyloid Protein in Patients Undergoing Long-Term Hemodialysis. *N. Engl. J. Med. 314*, 585–586.

562 22. Nakajima, K., Ogi, H., Adachi, K., Noi, K., Hirao, M., Yagi, H., and Goto, Y. (2016)
563 Nucleus factory on cavitation bubble for amyloid β fibril. *Sci. Rep. 6*, 22015, 1–10.

564 23. Adachi, M., So, M., Sakurai, K., Kardos, J., and Goto, Y. (2015) Supersaturation-limited
565 and unlimited phase transitions compete to produce the pathway complexity in amyloid
566 fibrillation. *J. Biol. Chem. 290*, 18134–18145.

567 24. Woody, R. W. (1995) Circular dichroism. *Methods Enzymol. 246*, 34–71.

568 25. Foley, J., Hill, S. E., Miti, T., Mulaj, M., Ciesla, M., Robeel, R., Persichilli, C.,
569 Raynes, R., Westerheide, S., and Muschol, M. (2013) Structural fingerprints and their
570 evolution during oligomeric vs. oligomer-free amyloid fibril growth. *J. Chem. Phys. 139*,
571 121901, 1–12.

572 26. Miti, T., Mulaj, M., Schmit, J. D., and Muschol, M. (2015) Stable, Metastable, and
573 Kinetically Trapped Amyloid Aggregate Phases. *Biomacromolecules 16*, 326–335.

574 27. Adachi, M., Noji, M., So, M., Sasahara, K., Kardos, J., Naiki, H., and Goto, Y. (2018)
575 Aggregation-phase diagrams of β2-microglobulin reveal temperature and salt effects on
576 competitive formation of amyloids versus amorphous aggregates. *J. Biol. Chem. 293*,
577 14775–14785.

578 28. Micsonai, A., Wien, F., Kernya, L., Lee, Y.-H., Goto, Y., Réfrégiers, M., and Kardos, J.
579 (2015) Accurate secondary structure prediction and fold recognition for circular dichro-
580 ism spectroscopy. *Proc. Natl. Acad. Sci. U.S.A. 112*, E3095–E3103.

581 29. Micsonai, A., Wien, F., Bulyáki, É., Kun, J., Moussong, É., Lee, Y.-H., Goto, Y.,
582 Réfrégiers, M., and Kardos, J. (2018) BeStSel: a web server for accurate protein sec-
583 ondary structure prediction and fold recognition from the circular dichroism spectra.
584 *Nucleic Acids Res. 46*, W315–W322.

30. Chatani, E., Lee, Y.-H., Yagi, H., Yoshimura, Y., Naiki, H., and Goto, Y. (2009) Ultrasonication-dependent production and breakdown lead to minimum-sized amyloid fibrils. *Proc. Natl. Acad. Sci. U.S.A. 106*, 11119–11124.

31. Hasecke, F., Miti, T., Perez, C., Barton, J., Schölzel, D., Gremer, L., Grüning, C. S. R., Matthews, G., Meisl, G., Knowles, T. P. J., Willbold, D., Neudecker, P., Heise, H., Ullah, G., Hoyer, W., and Muschol, M. (2018) Origin of metastable oligomers and their effects on amyloid fibril self-assembly. *Chem. Sci. 9*, 5937–5948.

32. Ries-Kautt, M. M., and Ducruix, A. F. (1989) Relative effectiveness of various ions on the solubility and crystal growth of lysozyme. *J. Biol. Chem. 264*, 745–748.

33. Nakajima, K., Nishioka, D., Hirao, M., So, M., Goto, Y., and Ogi, H. (2017) Drastic acceleration of fibrillation of insulin by transient cavitation bubble. *Ultrason. Sonochem. 36*, 206–211.

34. Jean, L., Lee, C., and Vaux, D. (2012) Enrichment of Amyloidogenesis at an Air-Water Interface. *Biophys. J. 102*, 1154–1162.

35. Hill, E. K., Krebs, B., Goodall, D. G., Howlett, G. J., and Dunstan, D. E. (2006) Shear Flow Induces Amyloid Fibril Formation. *Biomacromolecules 7*, 10–13.

36. Okumura, H., and Itoh, S. G. (2014) Amyloid Fibril Disruption by Ultrasonic Cavitation: Nonequilibrium Molecular Dynamics Simulations. *J. Am. Chem. Soc. 136*, 10549–10552.

37. Zeiger, B. W., and Suslick, K. S. (2011) Sonofragmentation of Molecular Crystals. *J. Am. Chem. Soc. 133*, 14530–14533.

38. Dear, A. J., Meisl, G., Šarić, A., Michaels, T. C. T., Kjaergaard, M., Linse, S., and Knowles, T. P. J. (2020) Identification of on- and off-pathway oligomers in amyloid fibril formation. *Chem. Sci. 11*, 6236–6247.

608 39. Lin, Y., Kardos, J., Imai, M., Ikenoue, T., Kinoshita, M., Sugiki, T., Ishimori, K.,
609 Goto, Y., and Lee, Y.-H. (2016) Amorphous Aggregation of Cytochrome c with Inher-
610 ently Low Amyloidogenicity Is Characterized by the Metastability of Supersaturation
611 and the Phase Diagram. *Langmuir 32*, 2010–2022.

612 40. Hasecke, F., Niyangoda, C., Borjas, G., Pan, J., Matthews, G., Muschol, M., and
613 Hoyer, W. (2021) Protofibril–Fibril Interactions Inhibit Amyloid Fibril Assembly by
614 Obstructing Secondary Nucleation. *Angew. Chem. Int. Ed. 60*, 3016–3021.

615 41. Nakajima, K., So, M., Takahashi, K., Tagawa, Y., Hirao, M., Goto, Y., and Ogi, H.
616 (2017) Optimized Ultrasonic Irradiation Finds Out Ultrastable Aβ1–40 Oligomers. *J.*
617 *Phys. Chem. B 121*, 2603–2613.

618 42. Enomoto, N., Sung, T. H., Nakagawa, Z. E., and Lee, S. C. (1992) Effect of ultrasonic
619 waves on crystallization from a supersaturated solution of alum. *J. Mater. Sci. 27*, 5239–
620 5243.

621 43. Enomoto, N., Akagi, J., and Nakagawa, Z. (1996) Sonochemical powder processing of
622 iron hydroxides. *Ultrason. Sonochem. 3*, 97–103.

623 44. Dang, F., Enomoto, N., Hojo, J., and Enpuku, K. (2009) Sonochemical synthesis of
624 monodispersed magnetite nanoparticles by using an ethanol–water mixed solvent. *Ultra-*
625 *son. Sonochem. 16*, 649–654.

626 45. Streets, A. M., and Quake, S. R. (2010) Ostwald Ripening of Clusters during Protein
627 Crystallization. *Phys. Rev. Lett. 104*, 178102–178106.

628 46. Zhang, Z., Wang, Z., He, S., Wang, C., Jin, M., and Yin, Y. (2015) Redox reaction
629 induced Ostwald ripening for size- and shape-focusing of palladium nanocrystals. *Chem.*
630 *Sci. 6*, 5197–5203.

631 47. Chiba, T., Hagihara, Y., Higurashi, T., Hasegawa, K., Naiki, H., and Goto, Y. (2003)
632 Amyloid fibril formation in the context of full-length protein: Effects of proline mutations
633 on the amyloid fibril formation of β2-microglobulin. *J. Biol. Chem. 278*, 47016–47024.

634 48. Biancalana, M., Makabe, K., Koide, A., and Koide, S. (2009) Molecular Mechanism of
635 Thioflavin-T Binding to the Surface of β-Rich Peptide Self-Assemblies. *J. Mol. Biol.*
636 *385*, 1052–1063.

637 49. Shahnawaz, M., Tokuda, T., Waragai, M., Mendez, N., Ishii, R., Trenkwalder, C., Mol-
638 lenhauer, B., and Soto, C. (2017) Development of a Biochemical Diagnosis of Parkinson
639 Disease by Detection of α-Synuclein Misfolded Aggregates in Cerebrospinal Fluid. *JAMA*
640 *Neurology 74*, 163–172.

641 50. Ikenoue, T., Lee, Y.-H., Kardos, J., Yagi, H., Ikegami, T., Naiki, H., and Goto, Y. (2014)
642 Heat of supersaturation-limited amyloid burst directly monitored by isothermal titration
643 calorimetry. *Proc. Natl. Acad. Sci. U.S.A. 111*, 6654–6659.

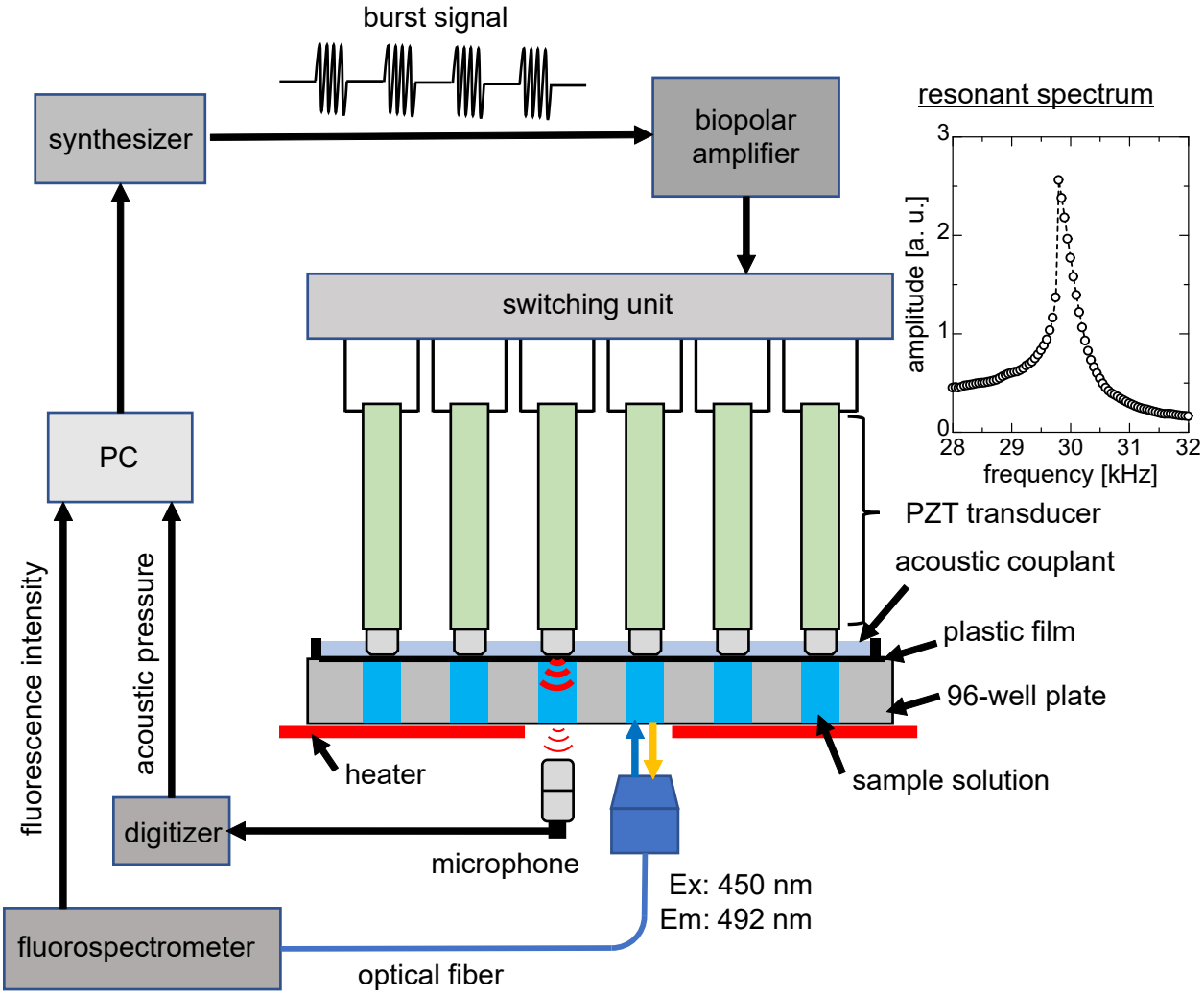

Figure 1: Schematic illustration of the laboratory-build ultrasonic instrument. The PZT transducer with the resonant frequency of 30 kHz is placed on each well of the 96-well plate with the sample solution with a volume of 198 μL. The sample solution is sealed by a plastic film. The ultrasound generated by the PZT transducer irradiates the sample solution through the acoustic couplant and the plastic film. The ultrasonic intensity in each sample solution is measured using the microphone beneath the microplate. By obtaining the resonant spectrum of each transducer as shown in the inset, the frequency of the burst signal applied to each transducer is individually determined.

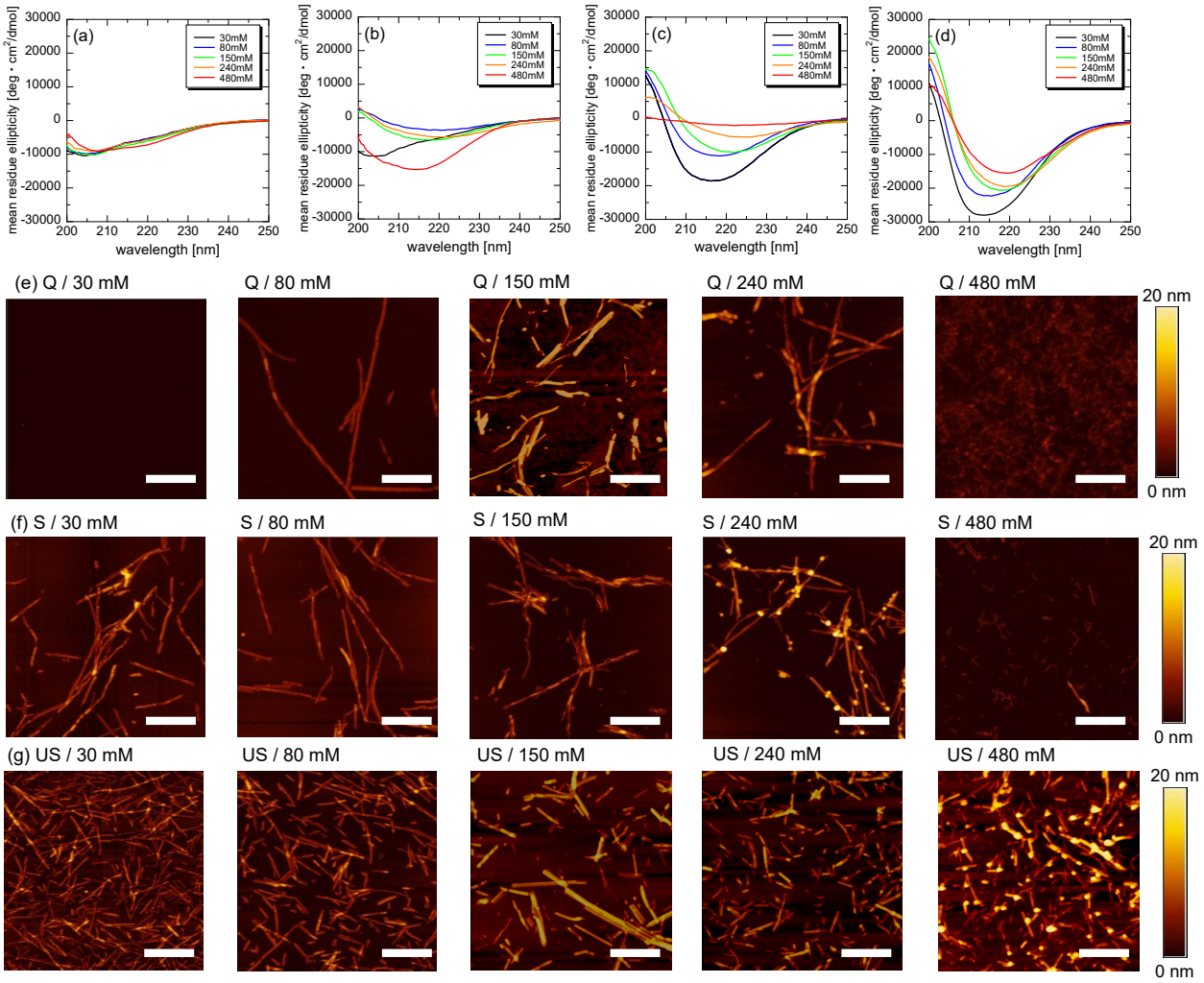

Figure 2: (a)-(d) The CD spectra of (a) initial acidic monomer solution, and the aggregates formed under (b) quiescence, (c) shaking, and (d) ultrasonication. (e)-(g) AFM images of the β2m aggregates formed under (e) quiescence, (f) shaking, and (g) ultrasonication with various salt concentrations, respectively. Q, S, and US are abbreviations of quiescence, shaking, and ultrasonication, respectively. The scale bars denote 500 nm. For all AFM images, the color scale was adjusted to be the same as indicated by the color scale bars (0 - 20 nm). Because the curvilinear fibrils shown in Q / 480 mM and S / 480 mM are thinner than the amyloid fibrils, the AFM images with a clearer contrast are shown in Figure S3b,c.

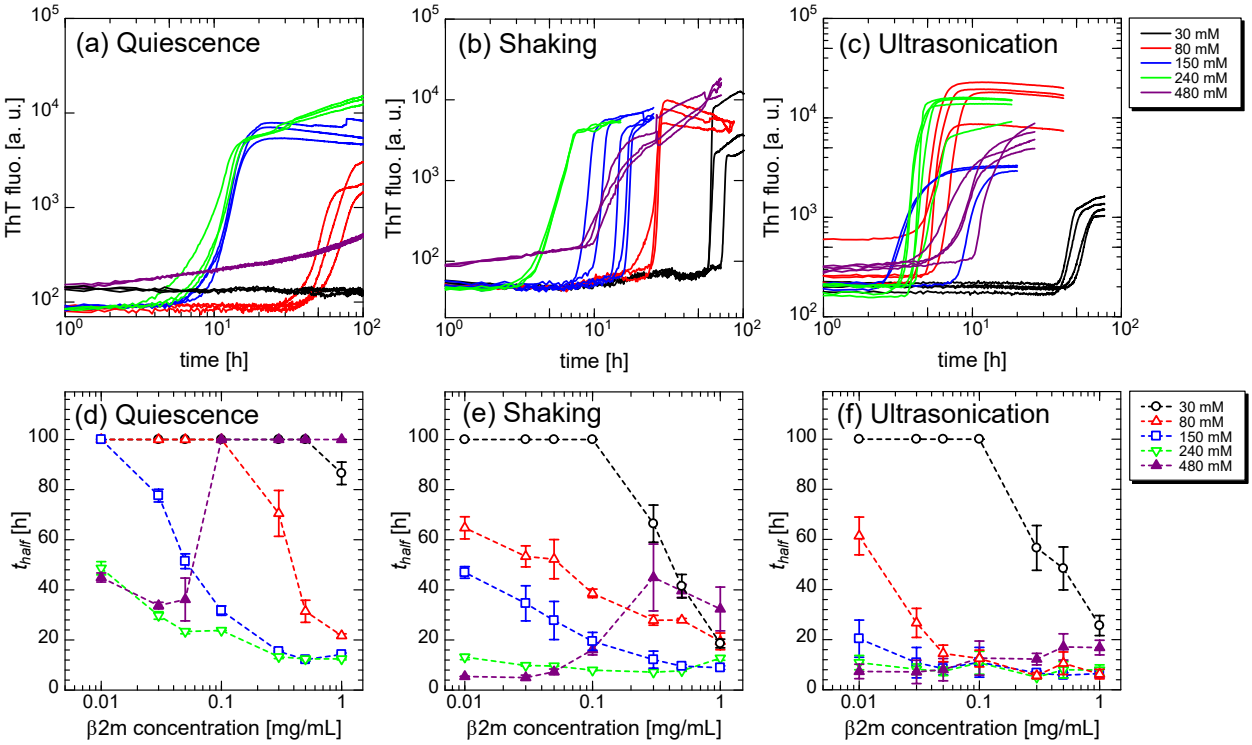

Figure 3: (a)-(c) The ThT time-course curves of the 0.3-mg/mL monomer solutions with various salt concentrations under (a) quiescence, (b) shaking, and (c) ultrasonication. (n >3) (d)-(e) Relationships between the half time (t_{half} values) for the fibril formation and β2m monomer concentration under (d) quiescence, (e) shaking, and (f) ultrasonication at various salt concentrations. The error bars denote the standard deviation among multiple solutions ($n > 3$).

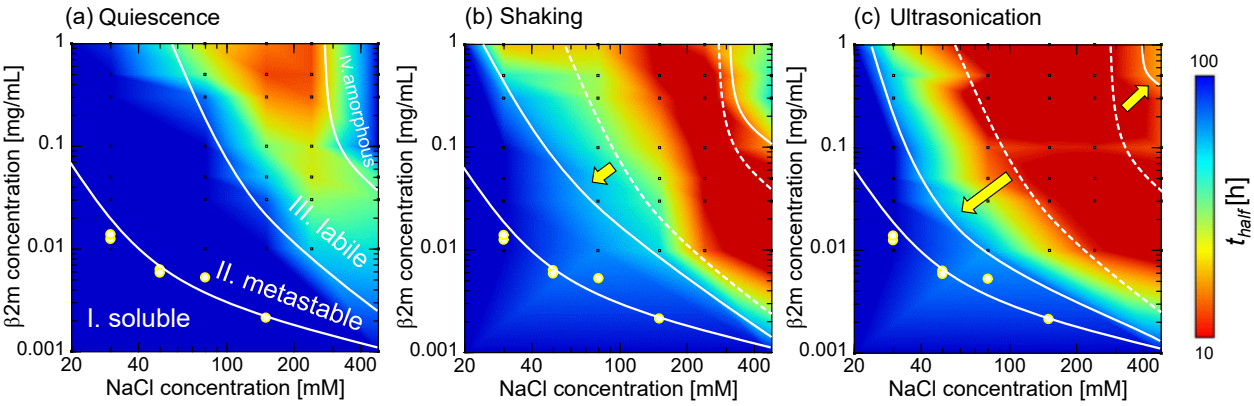

Figure 4: Half-time (t_{half}-value) heat maps of the aggregation reactions under (a) quiescence, (b) shaking, and (c) ultrasonication. The yellow dots denote the solubility of acidic β2m monomer at each salt concentration determined by the ultracentrifugation and ELISA assay (see Materials and Methods). The dot lines in (b) and (c) indicate the phase boundaries under quiescence which are varied under agitations.

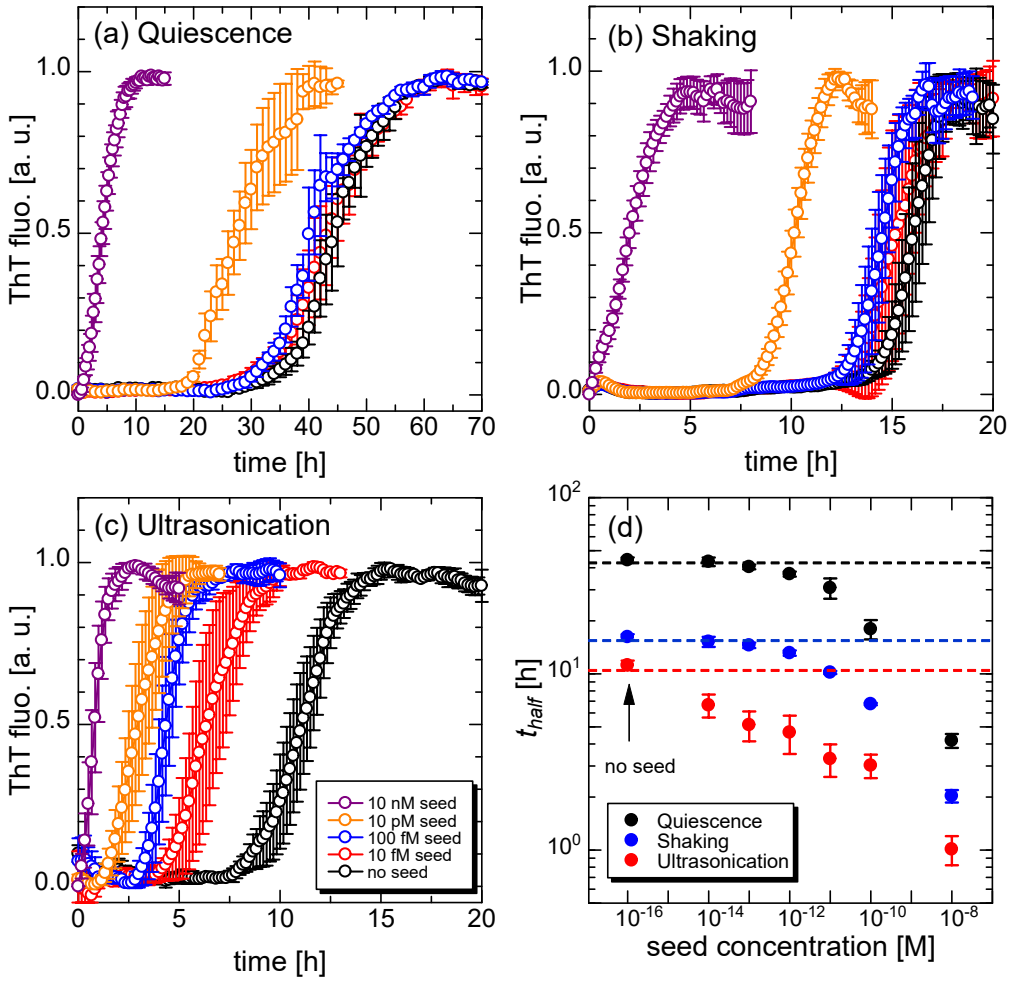

Figure 5: Time-course curves of the ThT fluorescence intensity of the samples with different seed concentrations under (a) quiescence, (b) shaking, and (c) ultrasonication, respectively. The color of each plot in the legend of (a) is common to (b) and (c). The error bars denote a deviation of the ThT intensity among multiple solutions ($n > 3$). (d) Relationship between the seed concentration and the t_{half} value under three different agitations. The error bars denote a standard deviation in the t_{half} value among multiple solutions ($n > 3$). The broken lines show a time of the average t_{half} minus the standard deviation of the sample without the seeds.

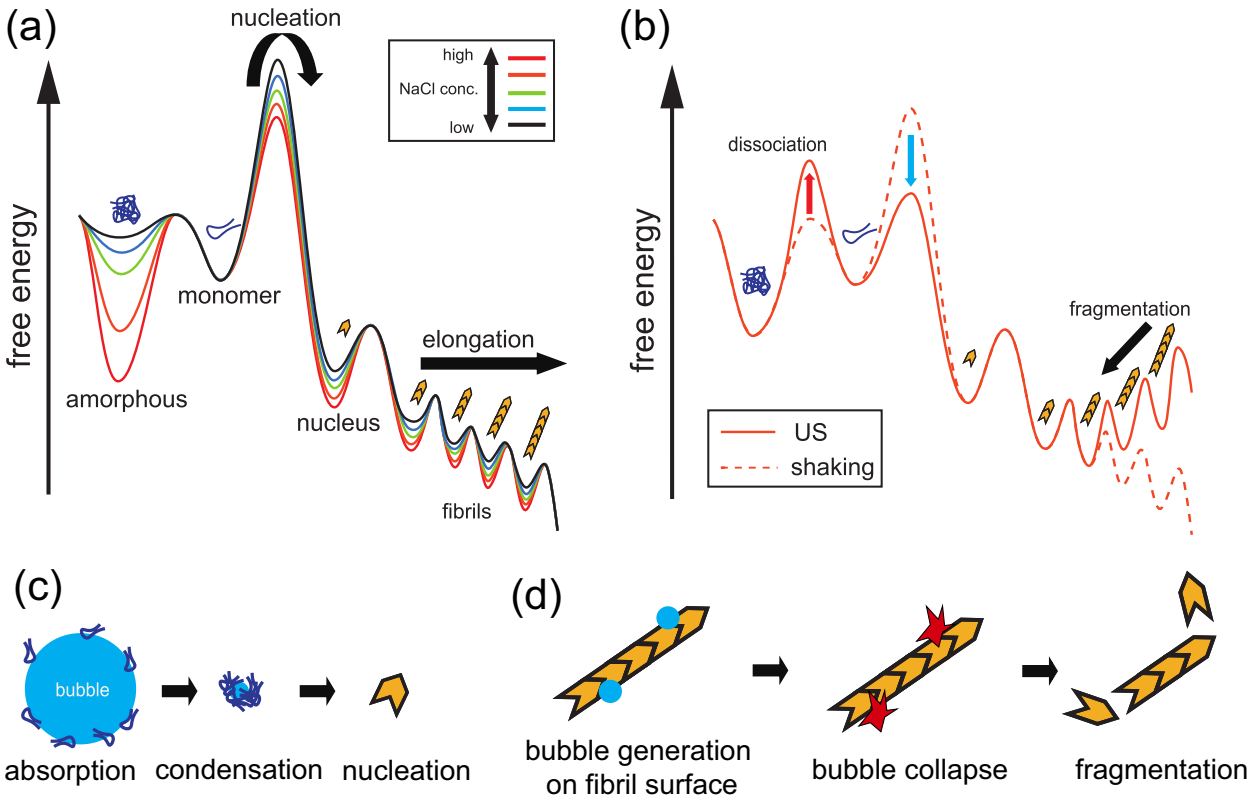

Figure 6: (a) Energy landscape of the aggregation reaction with different salt concentrations under quiescence and shaking. The colors of the curves denote the corresponding salt concentration qualitatively, as shown in the inset. (b) The difference in the energy landscape under ultrasonication (US, solid line) and shaking (broken line). The aggregation reaction starts from the monomer state. The right and left pathway from the monomer correspond to the fibril-formation and amorphous-aggregate-formation reactions, respectively. (c) Schematic illustration of the nucleation reaction catalyzed by ultrasonic cavitation. (d) Schematic illustration of the selective fragmentation of the mature fibrils by ultrasonic cavitation.

Table 1: Summary of resultant morphology of β2m with various NaCl concentrations and agitations. A. A. is an abbreviation of amorphous aggregate.

NaCl [mM]	30	80	150	240	480
Quiescence	Monomer	Fibril	Fibril	Fibril+A. A.	A. A.
Shaking	Fibril	Fibril	Fibril	Fibril+A. A.	A. A.
Ultrasonication	Fibril	Fibril	Fibril	Fibril	Fibril+A. A.

Graphical TOC Entry

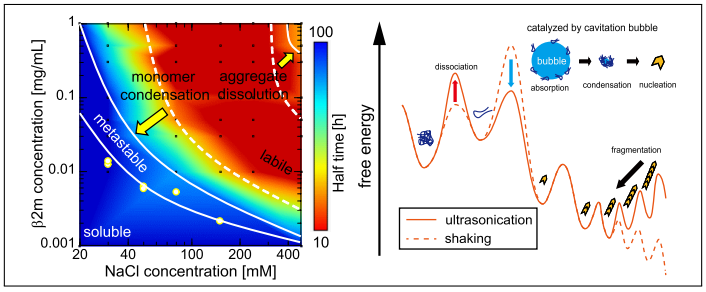

Supporting Information for

Half-time heat map reveals ultrasonic effects on morphology and kinetics of amyloidogenic aggregation reaction

Kichitaro Nakajima[†], Hajime Toda[¶], Keiichi Yamaguchi[†], Masatomo So[‡], Kensuke Ikenaka[§], Hideki Mochizuki[§], Yuji Goto[†], and Hirotsugu Ogi[*,¶]

† Global Center for Medical Engineering and Informatics, Osaka University, Suita, Osaka 565-0871, Japan

¶ Graduate School of Engineering, Osaka University, Suita, Osaka 565-0871, Japan

‡ Astbury Centre for Structural Molecular Biology, University of Leeds, Leeds LS2 9JT, UK

§ Department of Neurology, Graduate School of Medicine, Osaka University, Suita, Osaka 565-0871, Japan

*E-mail: ogi@prec.eng.osaka-u.ac.jp

Table of Content

SI Appendix 1. Reproducible amyloid-fibril assay using laboratory-built ultrasonic instrument

In the amyloid-fibril assays, the reaction kinetics is often discussed using the half time (i.e., t_{half})[1,2], which is the time when the ThT fluorescence intensity becomes the half its maximum. Because the t_{half} value varies widely even among the identical assays due to the high energy barrier for the nucleation[3], achieving a high reproducibility is challenging in an amyloid-fibril assay. Especially for ultrasonication, precise control of the fibril-formation reaction is very difficult because the reaction is highly sensitive to the acoustic field[3,4]. We here improved the ultrasonic instrument developed previously[2] to overcome the difficulty in the reproducibility of the assay as demonstrated below.

The fibril-formation reaction of the β2m monomer solution is monitored with a time-course of the ThT fluorescence intensity as shown in Figure S1. Under quiescence, the ThT intensity starts increasing after a 20-h lag time and reaches a plateau at 40 h. The AFM image of a sample incubated for 50 h under quiescence shows the typical fibril morphology (Figure 2e, Main text). By shaking, the lag time is shortened to ~10 h. In addition, the ThT intensity precipitously increases after the lag time compared to quiescence. The resultant fibrils are shown in Figure 2f (Main text). The lag phase and following evolution phase correspond to the nucleation and fibril elongation phases, respectively[5]. Thus, shaking accelerates both the nucleation and elongation reactions of the fibril formation. By ultrasonication, the fibril formation is further accelerated. The resultant fibrils are shorter than those formed under quiescence and shaking (Figure 2g, Main text). The difference in the morphology of the formed aggregates is discussed in detail in the following section.

The t_{half} value of the quiescent assay is 31.5±0.2 h, which varies with the coefficient of variation (CV) value of 0.6%. The CV value is significantly smaller than those with agitations: The CV value of the shaking assay is 10% (t_{half} = 11.1±1.1 h). For ultrasonication, our previous value was 22%[2], being less reproducible than shaking. In this study, we adopted the acoustic couplant to improve the stability of the contact between the PZT transducer and plastic film on the sample solutions. Also, we removed external forces applied to each transducer for the acoustical contact except for its own weight. Consequently, the ultrasonication assay shows the t_{half} value of 6.8±0.8 h (CV=12%) in this study. This improved CV value of the ultrasonication assay is comparable to that in the shaking assay, contributing to the following systematic investigation of the aggregation reactions.

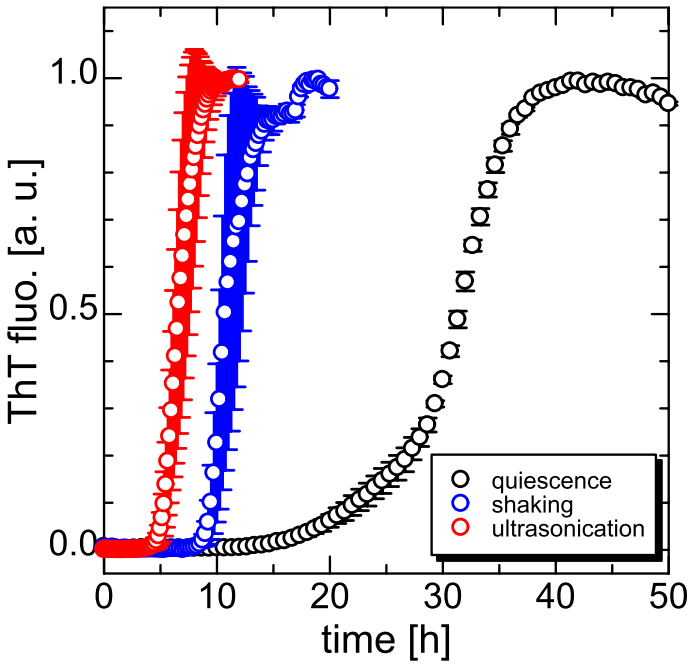

Figure S1. Time-course curves of the ThT fluorescence intensity of the 0.3-mg/mL β2m monomer solutions with 150-mM NaCl with quiescence (black circles), shaking (blue circles), and ultrasonication (red circles). The ThT fluorescence measurement was performed for the multiple solutions (n > 3). The error bars denote a standard deviation of the ThT intensity at each time among multiple solutions (n > 3).

SI Appendix 2. Detailed analysis of the AFM images

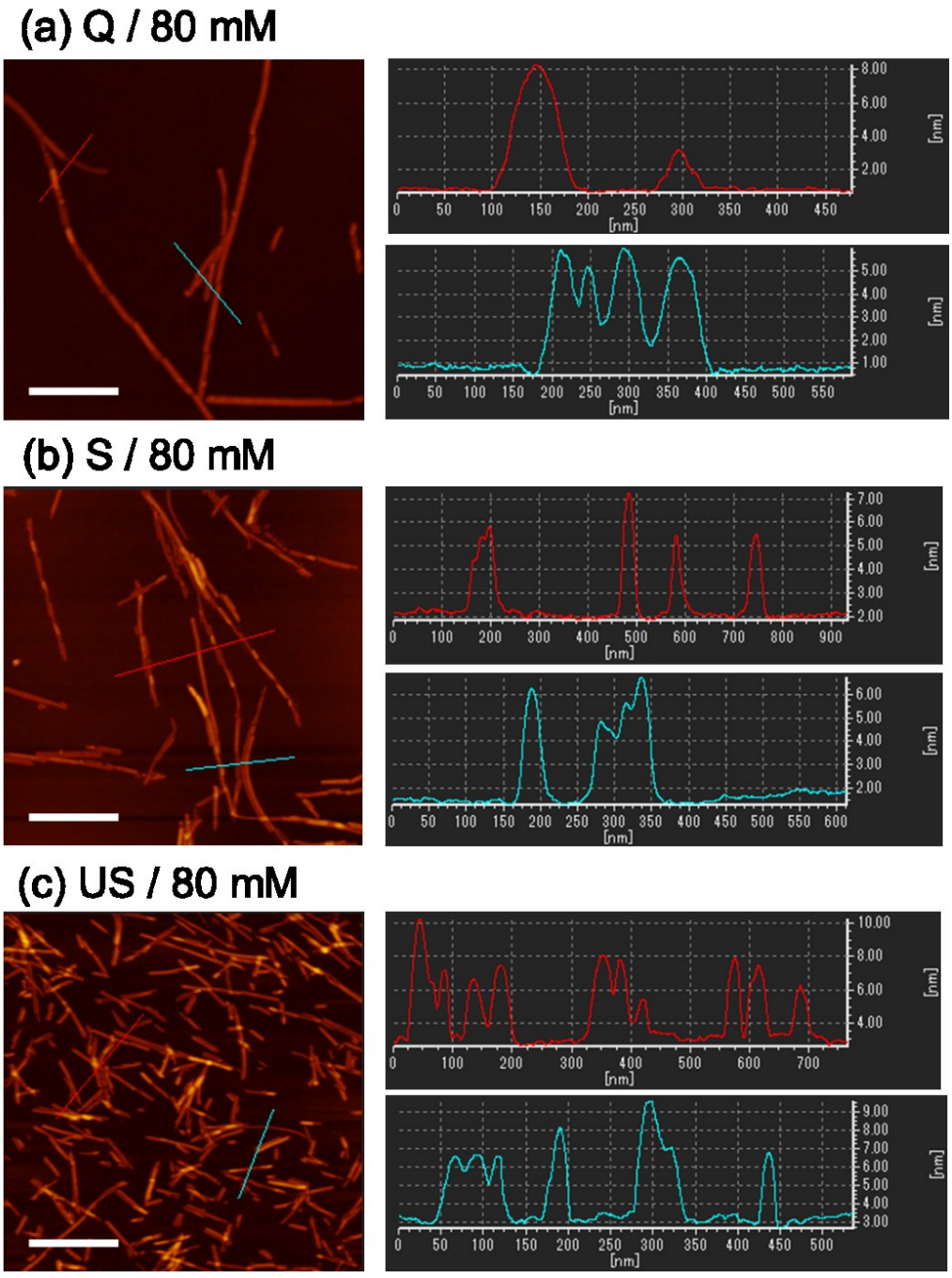

Figure S2. AFM images of the fibrils formed in the solution with the salt concentration of 80 mM under (a) quiescence, (b) shaking, and (c) ultrasonication, respectively. For each sample, the left panel shows the AFM image with a 500-nm scale bar. The red and cyan lines indicate the lines analyzed their cross-sectional profile as shown in the right panels. Under all agitations, the fibrils with the height between 5 and 10 nm formed.

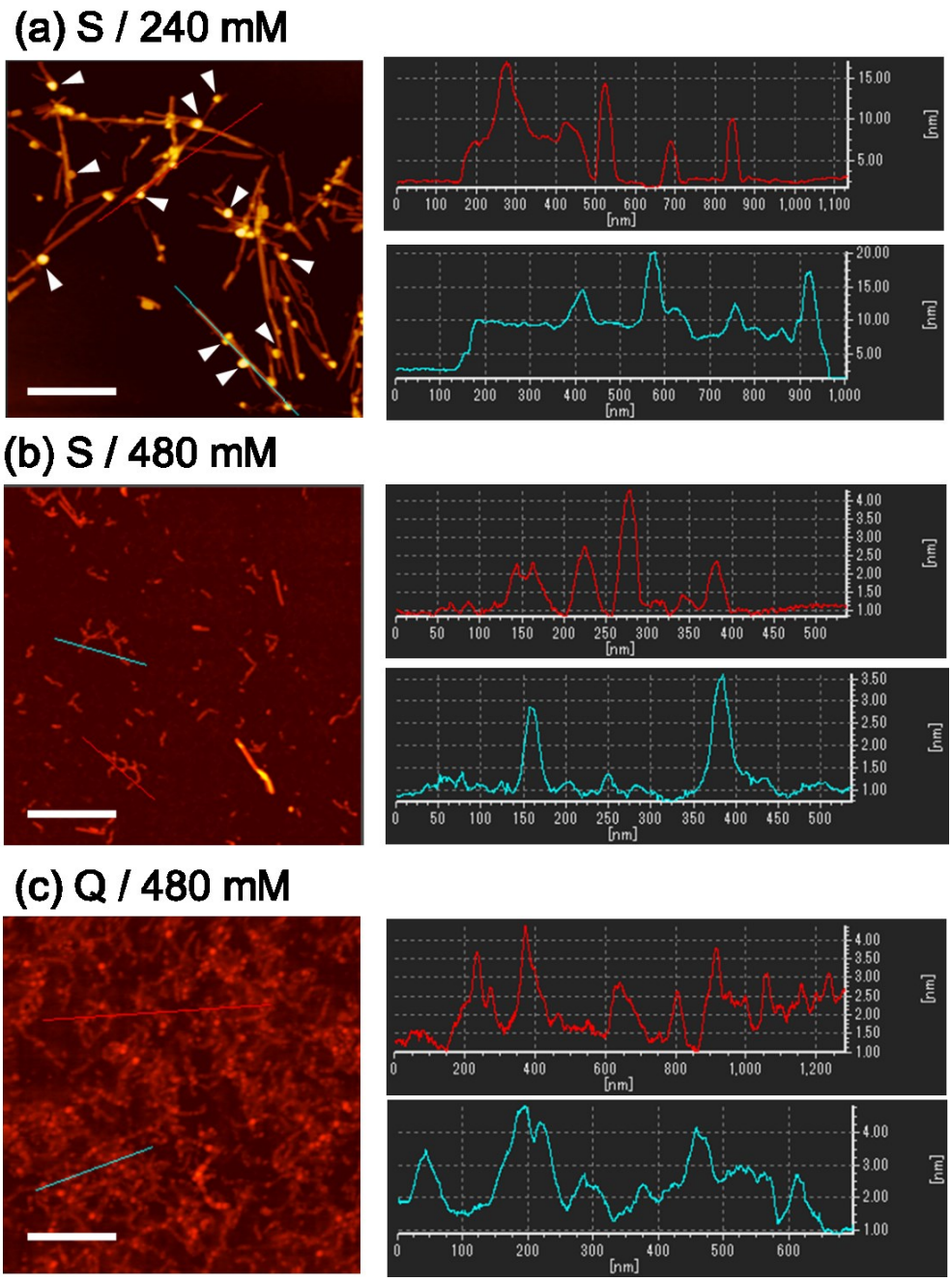

Figure S3. (a) The AFM image of the aggregates formed in the solution with the salt concentration of 240 mM under shaking. The white arrows in the left panel indicate the globular aggregates attached on the fibril surface. As shown in the right panels, the globular aggregates with the height of ~10 nm are attached on the fibrils with the height ~8 nm. (b),(c) The AFM images of the amorphous aggregates (curvilinear fibrils) formed in the solution with the salt concentration of 480 mM under (b) shaking and (c) quiescence. The height of the aggregates is less than 4 nm, being different from the fibrils shown in Figure S2.

SI References

[1] Shahnawaz, M.; Tokuda, T.; Waragai, M.; Mendez, N.; Ishii, R.; Trenkwalder, C.; Mollenhauer, B.; Soto, C. Development of a Biochemical Diagnosis of Parkinson Disease by Detection of a-Synuclein Misfolded Aggregates in Cerebrospinal Fluid. *JAMA Neurol.* **2017**, *74*, 163-172.

[2] Nakajima, K.; Noi, K.; Yamaguchi, K.; So, M.; Ikenaka, K.; Mochizuki, H.; Ogi, H.; Goto, Y. Optimized Sonoreactor for Accelerative Amyloid-Fibril Assays through Enhancement of Primary Nucleation and Fragmentation. *Ultrason. Sonochem.* **2021**, *73*, 105508.

[3] Umemoto, A.; Yagi, H.; So, M.; Goto, Y. High-throughput Analysis of Ultrasonication-Forces Amyloid Fibrillation Reveals the Mechanism Underlying the Large Fluctuation in the Lag Time. *J. Biol. Chem.* **2014**, *289*, 27290-27299.

[4] Nakajima, K.; Ogi, H.; Adachi, K.; Noi, K.; Hirao, M.; Yagi, H.; Goto, Y. Nucleus Factory on Cavitation Bubble for Amyloid β Fibril. *Sci. Rep.* **2016**, *6*, 22015.

[5] Morris, A. M.; Watzky, M. A.; Agar, J. N.; Finke, R. G. Fitting Neurological Protein Aggregation Kinetic Data via a 2-step, Minimal/"Ockham's Razor" Model: the Finke-Watzky Mechanism of Nucleation followed by Autocatalytic Surface Growth. *Biochemistry* **2008**, *47*, 2413-2427.